Oceanic Maintenance of Atmospheric Blocking in Wintertime in the North Atlantic

Jamie Mathews, [a] Arnaud Czaja,[a]

[a] *Imperial College London*

Corresponding author: Jamie Mathews, jamie.mathews19@imperial.ac.uk

ABSTRACT: The connection between atmospheric blocking over the North Atlantic and the diabatic influence of the Gulf Stream is investigated using potential vorticity and moist potential vorticity diagnostics in the ERA5 reanalysis data set during wintertime (1979 - 2020). In line with previous research, the reliance atmospheric blocking has on turbulent heat fluxes over the Gulf Stream and its extension, for induction and maintenance, is shown to be significant. The air-sea heat flux generates negative potential vorticity air masses in the atmospheric boundary layer. These air masses subsequently contribute to the block's negative potential vorticity anomaly at upper levels through ascending motion in the warm conveyor belt. It is shown that the block's size and frequency partially depends on oceanic preconditioning via anomalous oceanic heat transport and heat content, prior to the blocking event, both of which allow for stronger turbulent heat fluxes. It is further hypothesized that the block feeds back positively on itself through the advection of cold dry air over the Gulf Stream, sustaining this air-sea interaction. This in turn decreases ocean heat content, eventually halting this air-sea interaction and severing the atmospheric block from its maintenance pathway.

1. Introduction

As described by Woollings et al. (2018), atmospheric blocking refers to a persistent, quasi-stationary weather system in mid to high latitudes that disrupts the usual westerly flow. These blocks can be responsible for localised extreme high temperatures in the summer and non-local extreme cold temperatures in the winter, as demonstrated, for example, by Pfahl and Wernli (2012). Attempts to project oceanic influence on such large-scale atmospheric dynamics date back to Bjerknes (1964). He conjectured that the atmosphere drives the majority of short-term inter-annual sea surface temperature (SST) variability, while the ocean is responsible for longer-term variability. More recently, Häkkinen et al. (2011) demonstrated that decades marked by a heightened frequency of atmospheric blocks align with warmer subpolar oceans and weaker ocean gyres as a result of wind-driven forcing. This aligns with reduced heat removal within the subpolar gyre, subsequently contributing to warmer waters, as well as an increased turbulent heat flux (THF) from the Gulf Stream extension to the atmosphere. These observations collectively indicate the influence of atmospheric forcing on the ocean. In terms of the atmospheric response to changes in SSTs, O'Reilly and Czaja (2015) for the North Pacific, and O'Reilly et al. (2016) for the North Atlantic, showed that the state of SST fronts affects the frequency of atmospheric blocks on annual and sub-seasonal timescales, respectively. Furthermore, Famooss Paolini et al. (2022) suggested that the effects of the SST front on these blocks can only be observed with increased model resolution.

In order to accurately establish a connection between oceanic conditions and atmospheric blocks, it is crucial to utilize comparable parameters. Potential vorticity (PV) is a scalar quantity conserved by the flow in the absence of heating or friction. As defined by Schwierz et al. (2004), an atmospheric block is a negative PV anomaly in the upper troposphere that surpasses a certain amplitude, size, overlap, and stationarity threshold. Therefore, a direct comparison can be drawn between the generation of PV anomalies through diabatic air-sea interactions and atmospheric blocking indices. Furthermore, the PV impermeability theorem from Haynes and McIntyre (1990) asserts that PV substance remains constant across isentropic surfaces unless it encounters a boundary, such as the air-sea interface. In this context, PV can be introduced into the system, thereby influencing the fluid dynamics. By analyzing diabatic processes within the atmospheric boundary layer, Vannière et al. (2016) demonstrated that negative PV air masses are produced in the cold sector of a cyclone,

primarily through large to heat fluxes from the ocean to the atmosphere. These heat fluxes diminish the static stability within the boundary layer to such a magnitude and consistency that convection cannot sufficiently act to stabilize the temperature profile. Consequently, this results in a persistent negative PV signature at low levels of the troposphere. This finding is reinforced by Attinger et al. (2019), who extensively elucidated the role of individual diabatic processes in extratropical cyclones.

The heat flux from the ocean to the atmosphere does not only affect the PV of the atmosphere, but also the heat content of the ocean. Cayan (1992) noted that these heat fluxes exhibit a negative correlation with the rate of SSTs. While SST anomalies are primarily driven by stochastic atmospheric forcing as shown by Frankignoul and Hasselmann (1977), they are also altered by oceanic temperature advection, entrainment of the oceanic mixed layer and mixing (e.g. Frankignoul 1985 and more recently Bishop et al. 2017). The strength of these air-sea interactions is primarily due to the difference in air-sea temperatures and hence any buildup of oceanic heat has an effect on the strength of these fluxes, as observed for example by Kelly et al. (2010). The depth of the mixed layer in the ocean also determines how much thermal inertia these SST anomalies have. The deep mixed layer in the winter (Kraus and Turner 1967) slows down temperature change due to air-sea interactions (Cayan 1992) and acts as a heat reservoir for the atmosphere.

The importance of diabatic processes for atmospheric blocks is beginning to be understood. Pfahl et al. (2015) showed that 30-45% of the air mass involved in atmospheric blocks has undergone at least 2K of latent heating. Additionally, as shown by Yamamoto et al. (2021), these blocks source 28%-55% of their moisture for diabatic heating from the ocean, indicating that 11%-23% of blocking particles originate from oceanic pathways. Additionally, 88% of the along-trajectory potential temperature variability of these particles is explained by their accumulated THF (Yamamoto et al. 2015). A portion of this heating occurs along the fast warm ascending air stream in the cyclone known as the warm conveyor belt (WCB). After the particle's ascent, the diabatically modified air mass is deposited in the upper troposphere on the western flank of the block, advecting negative PV anomalies against the eastward background flow (Steinfeld and Pfahl 2019). A previous study by Steinfeld et al. (2020) showed that restraining the latent heating along the WCB resulted in some blocks experiencing a reduction of size, amplitude and duration, while others did not develop at all. Clearly the next step in understanding this diabatic contribution to

atmospheric blocking is to extend our gaze to the ocean, as both a source of negative PV air masses, and thus a source of negative PV anomalies, via surface sensible heat flux (SSHF), and a source of moisture for WCB ascent via surface latent heat flux (SLHF).

In this study we bring the discussion further. We demonstrate, employing the novel perspective provided by a moist PV framework, that the diabatic influence on wintertime North Atlantic blocks is not only a result of stronger air-sea interactions over the Gulf Stream and its extension, but also that oceanic preconditioning through heat advection and heat content anomalies affect both the block's size and frequency in the North Atlantic basin. This paper is structured as follows. In section 2 we describe the data and methods. Analysis is done in section 3. Details of the method and orders of magnitude are discussed in 4, followed by our conclusions in section 5.

2. Method

The results presented in this paper are derived from ERA5 data spanning from 1979 to 2020 (ERA5, Hersbach et al. (2020)). Heat transport data from the RAPID array is utilized for the period between 2004 and 2018, as calculated by McCarthy et al. (2015). Additionally, the top 300 meters of heat content data is obtained from Argo measurements covering the same period from 2004 to 2018 (Argo (2023)).

The blocking mask was computed following the method outlined by Schwierz et al. (2004) utilizing ERA5 data. To prepare the data for this algorithm, the PV field was averaged within the 150hPa to 500hPa range. Subsequently, a 31-day running mean climatology was subtracted from the signal to generate PV anomalies in the upper troposphere.

Moist PV was calculated by substituting equivalent potential temperature for potential temperature in Ertel's PV equation (Gill 1982). The calculation of equivalent potential temperature follows the method outlined by Bolton (1980).

For composite analysis, we utilized the moving block bootstrap technique as introduced by Wilks (1997) to preserve both temporal and spatial correlations within the fields. We employed five hundred bootstrap samples. The size of the resample block was based on the length of time required for the observed field to decorrelate. For example, when calculating a blocking frequency composite, the blocking field was resampled in blocks of 12 days. This duration was chosen as it was approximately the time needed for any random point in the blocking field to become

decorrelated with itself. Subsequently, the composite calculation was performed on each bootstrap sample, resulting in a distribution of randomly generated composites. From this distribution, the false discovery rate could be extracted, providing the 95% confidence interval (Wilks 2016).

Significance values for cross-correlation analysis are determined as follows. Two time series, each the same length as the observed time series, were generated using a first-order autoregressive model with the same autocorrelation characteristics as the observed time series. Then a cross-correlation was performed between these two synthetic time series. This process was repeated 500 times, generating a distribution of the cross-correlation coefficients. The significance interval was then determined from this distribution.

NAME	DATA SET	UNITS	FREQUENCY	LOCATION	DESCRIPTION
Heat Flux	ERA5	Wm^{-2}	6 hourly	Air-sea interface	Mean of the turbulent heat flux field inside the $350Wm^{-2}$ DJF turbulent heat flux climatology contour (orange contour, Fig. 3)
PV	ERA5	PVU	6 hourly	950hPa	Mean of the PV field inside the $350Wm^{-2}$ DJF turbulent heat flux climatology contour (orange contour, Fig. 3)
Block On	ERA5	Dimensionless	6 hourly	150hPa - 500 hPa	Binary time series indicating the presence of a block inside the 7.5% DJF blocking frequency climatology contour (green contour, Fig. 3)
Block Area	ERA5	m^2	6 hourly	150hPa - 500 hPa	The total area of the block inside the 7.5% blocking frequency climatology in DJF (green contour, Fig. 3)
Heat Content	ARGO	J	Monthly	Top 300m of ocean	Oceanic heat content integrated inside the $350Wm^{-2}$ DJF turbulent heat flux climatology contour (orange contour, Fig. 3)
Heat Transport	RAPID	W	12 hourly	Oceanic profile at $26N$	Heat transport through the Straits of Florida at $26N$

TABLE 1. The collection of time series used in this analysis, with a description of which data set they belong to, their units, frequency, location and how they were calculated.

The time series employed in this study, as detailed in Table 1, were deseasonalised. This process involved calculating the average value for each specific time step within a year (e.g., January 1st, 0600hrs), applying a 30 day running average to that seasonal cycle and then subtracting it from the respective time series to eliminate seasonal variations. This was done to eliminate correlations arising from seasonal variability in these variables. Additionally, linear detrending was applied to

all time series to limit the the influence of long term signals such as multi-decadal variability or anthropogenic forcing.

3. Results

Synoptic and Climatological Conditions

To motivate our analysis, we first describe the synoptic situation of a cyclonic event that occurred on January 18^{th} 2020. Fig. 1 shows the PV field (coloured field) for the preconditioning (top panel), induction (middle panel) and maintenance (bottom panel) processes of an atmospheric block over the North Atlantic. The left panels display a cross section of these events, with the position of the cross section indicated by the dotted white line in the corresponding right panels. The right panels illustrate the lower troposphere average (900hPa - 975hPa) of this field. Focusing on the right panels, the purple and black colors indicate regions of negative PV air mass, primarily located in the cold sector of the cyclones and its wake as it moves over the North Atlantic. Although this negative PV air-mass is unstable (Hoskins 1974), it pools in the wake of the cyclone, weakening with its distance from the cold sector. As the cyclone moves over the Gulf Stream, this negative PV region in the cold sector corresponds to areas of extreme THF as shown by the orange contour. The preference this heat flux has to warmer waters is clearly seen in Fig. 1, in which the THF contour roughly coincides with the Gulf Stream surface warm core. Note that negative PV is also present ahead of the cyclone and to the southeast of the cyclone's cold front. This negative PV signal was seen in the cold sector of a previous cyclone (not shown), which can now be observed decaying southwest of the Irish coast.

The middle panel in Fig. 1 depicts the induction of a block with the white contour indicating the blocking mask. This corresponds to the outflow of the WCB as illustrated by the red stippled contours which depict upward velocities at 500hPa where $\omega < -1\text{Pas}^{-1}$. Moreover, there is northward advection of upper tropospheric anticyclonic air contributing to the generation of this negative PV anomaly (not shown). This is a typical situation for many block's genesis over the North Atlantic, and is in agreement with Steinfeld and Pfahl (2019).

Focusing on the left panels, the presence of negative PV air masses is primarily within the atmospheric boundary layer, as denoted by the dashed red line, but also present in thin filaments extending from the boundary layer to the upper troposphere. These filaments are co-located with

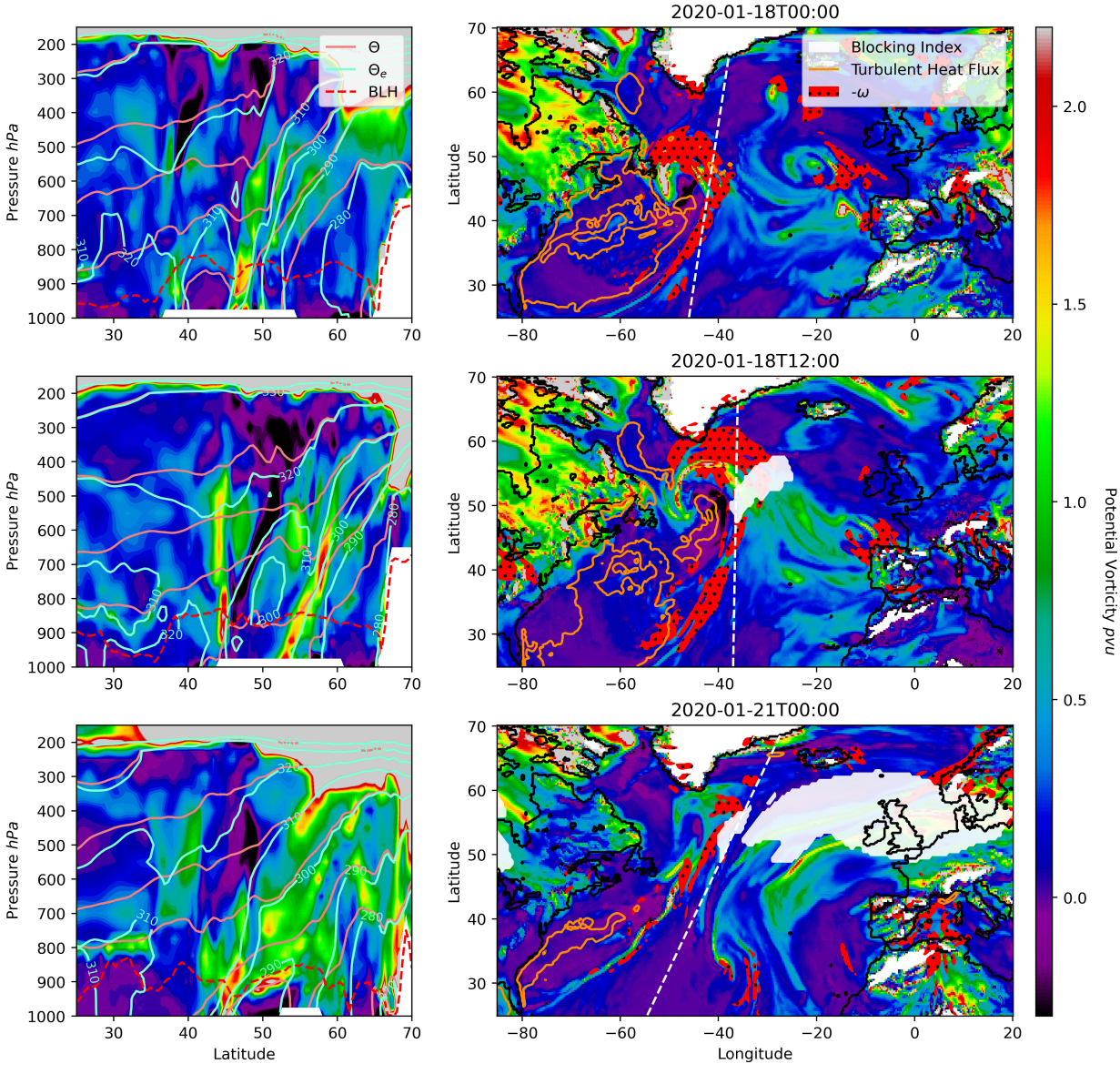

FIG. 1. PV section (left) and PV averaged between 900-975 hPa (in PVU, 1 PVU = 10^{-6} Km^2 s^{-1} kg^{-1}) (right) for a blocking event starting on January 18^{th}, 2020. In the left panels, the light red, light blue, and dashed red contours indicate the potential temperature, equivalent potential temperature, and boundary layer height respectively. In the right panels, the white contour indicates the blocking mask, the orange contours show the 500 Wm^{-2}, 1000 Wm^{-2}, and 1500 Wm^{-2} turbulent heat flux, and the red stippled contour shows upward velocities at 500 hPa where $\omega < -1$ Pa s^{-1}. The dashed white line indicates where the section is taken.

the ω contours in the right panels, and hence are transported upwards at 500hPa. This observation

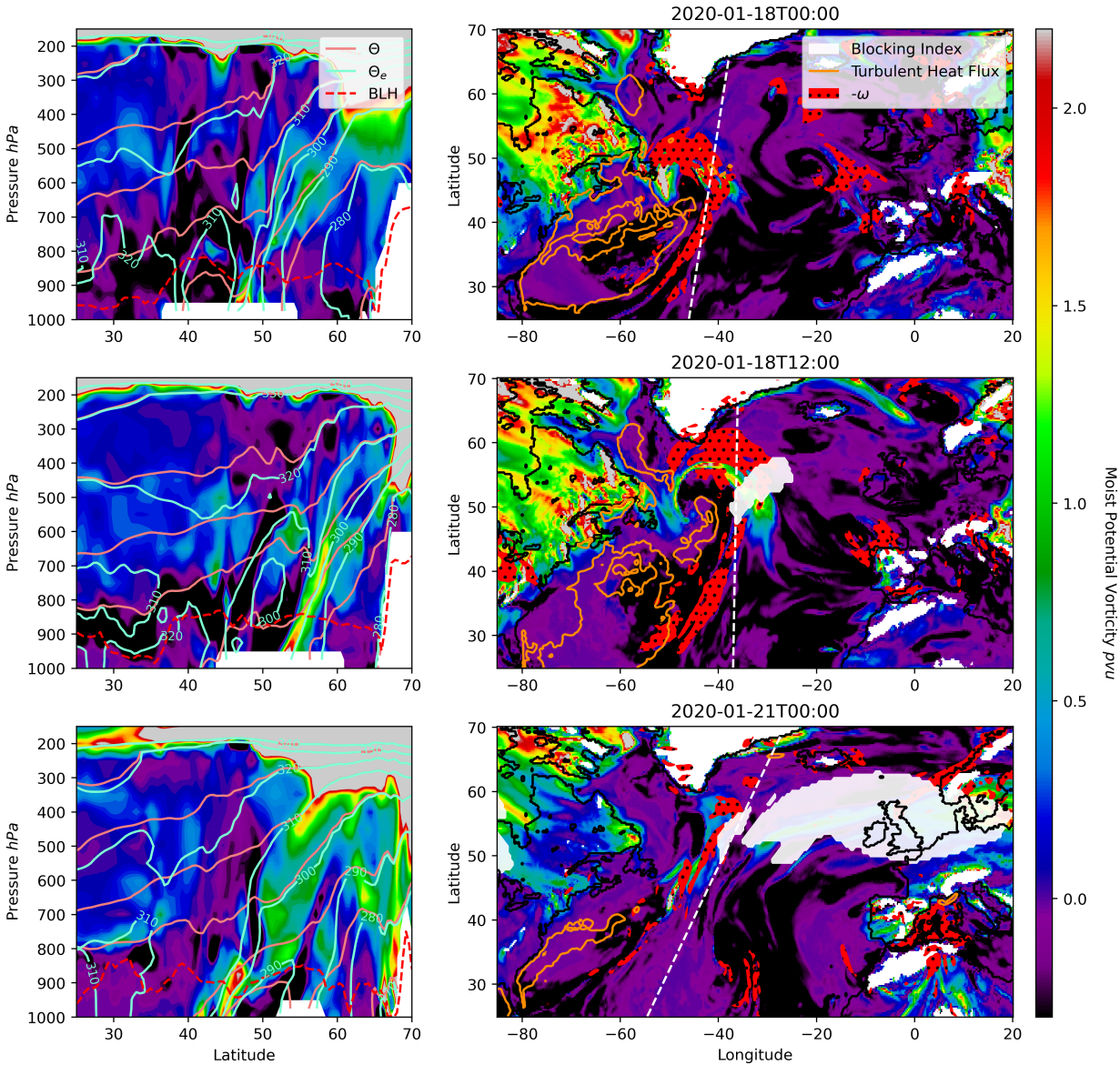

FIG. 2. As in Fig. 1 but now showing moist PV.

suggests an injection of negative PV air masses from the boundary layer into the upper troposphere which contributes to the negative PV anomaly of this atmospheric block.

The bottom panel depicts a typical maintenance process in which a subsequent cyclone deposits a diabatically modified air mass on the western flank of the block, thus advecting negative PV anomalies westward and preventing the block from decaying (Holmberg et al. 2022). This is seen in the detached white contour which has just appeared at this time step and merges with the larger contour in the next time step (not shown).

Focusing on diabatic effects, we analyse this event from a moist PV framework, as shown in Fig. 2. As discussed in Bennetts and Hoskins (1979), moist PV can only be changed by diabatic effects other than latent heat release, and when the angle between the moist and dry isentropes in the horizontal plane is non-zero. For clarity, PV calculated using dry isentropes will now be called "dry" PV. The right panels illustrate the ubiquitous presence of negative moist PV air masses over the North Atlantic, with the sole exception being along cyclonic fronts. Since moisture fluxes now influence equivalent potential temperature, and consequently moist PV, as demonstrated by Pauluis et al. (2010), we observe the additional impact of SLHF on the boundary layer moist PV. Therefore negative moist PV in the boundary layer has a larger magnitude when compared to "dry" PV, on the order of $O(1\text{PVU})$. In addition, as indicated by the light blue contours representing equivalent potential temperature, this moist PV undergoes minimal change during its ascent from the boundary layer to the upper troposphere along moist isentropes, as also observed by Martínez-Alvarado et al. (2014). Conversely, when examining the light red contours indicating potential temperature, we find, from a dry perspective, that the air mass along these filaments must experience at least 20K of heating in order to ascend from the boundary layer to the upper troposphere, a value consistent with observations by Madonna et al. (2014) in WCBs. It is worth noting that both the dry and moist isentropes converge with increasing height due to the scarcity of moisture at these pressure levels, which accounts for the similarities observed between PV and moist PV in Fig. 1 and 2 in the upper troposphere.

We now turn to the climatology. Fig. 3 shows the DJF (December, January, February) mean of both the THF and the PV at 950hPa. Positive THF indicates heat flux from the ocean to the atmosphere. This figure shows an increased THF along the warm core of the Gulf Stream and its extension, with the presence of low PV air masses above. The latter's presence extends to the continental shelf, into the Labrador Sea and Irminger Basin. It notably aligns with the positive THF pattern observed over the North Atlantic and demonstrates a distinct sensitivity to the demarcation between the continental shelf and the deep ocean.

Fig. 4 presents the DJF mean of the negative PV frequency throughout the troposphere. In the lower troposphere (bottom panels), there is a pronounced spatial signature that corresponds to the THF signature observed in Fig. 3. This signature weakens with increasing height. In the middle troposphere (middle panels), this signal diminishes, although it still displays a stronger presence

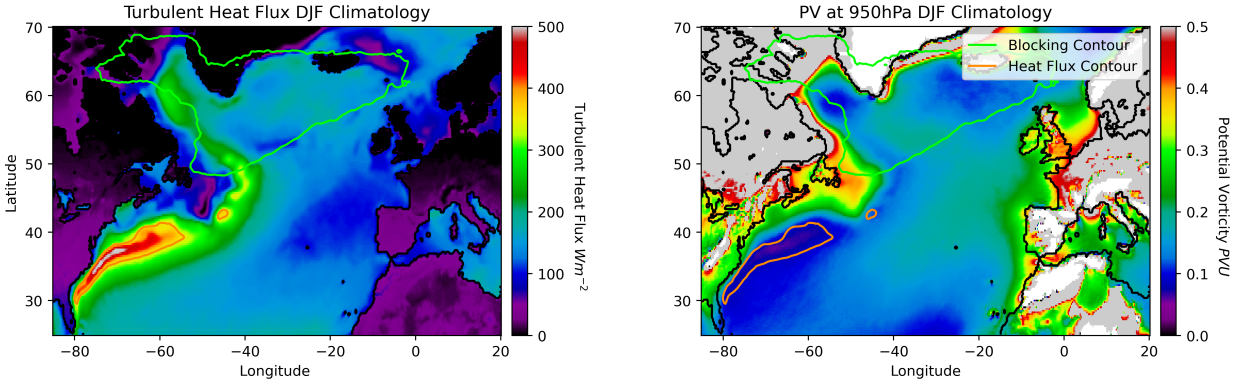

FIG. 3. DJF climatology of the THF and PV at 950hPa over the North Atlantic. The green and orange contours represent the 7.5% blocking frequency and the 350Wm^{-2} THF climatology during DJF, respectively.

over the storm track, before increasing again at 300hPa. The spatial pattern observed at 300hPa closely resembles the WCB climatology for DJF as observed by Madonna et al. (2014), depicted in their Fig. 4.

The white contours in Fig. 4 represent the frequency of negative moist PV. In contrast to the "dry" PV situation, negative moist PV is widespread in the lower troposphere and shows a gradual decrease towards the upper troposphere, where it aligns with the negative PV signal. It is worth noting that our moist PV diagnostic does not show this decrease in the middle troposphere, unlike that of "dry" PV. We interpret this results as reflecting the negligible effects of latent heating on moist isentropes (Pauluis et al. 2010) along the warm conveyor belt.

Cross correlation analysis between the heat flux and PV time series described in section 2 (refer to Table 1), confirms the influence of oceanic heat fluxes on boundary layer air (not shown). There is a minimum correlation of -0.54 between these two 6-hourly time series when the heat flux time series leads by 6 hours. This strengthens to a minimum of -0.74 when performing a one month running mean, having the strongest correlation with the heat flux time series leading by 42 hours. Expanding the moving average window leads to a reduced correlation between the two time series, highlighting that this phenomenon operates on timescales of approximately one month or less. This relationship is in agreement with Vannière et al. (2016) who shows that negative PV air masses are generated in the cold sector of cyclones through the reduction of static stability in the atmospheric boundary layer caused by strong upward air-sea heat fluxes.

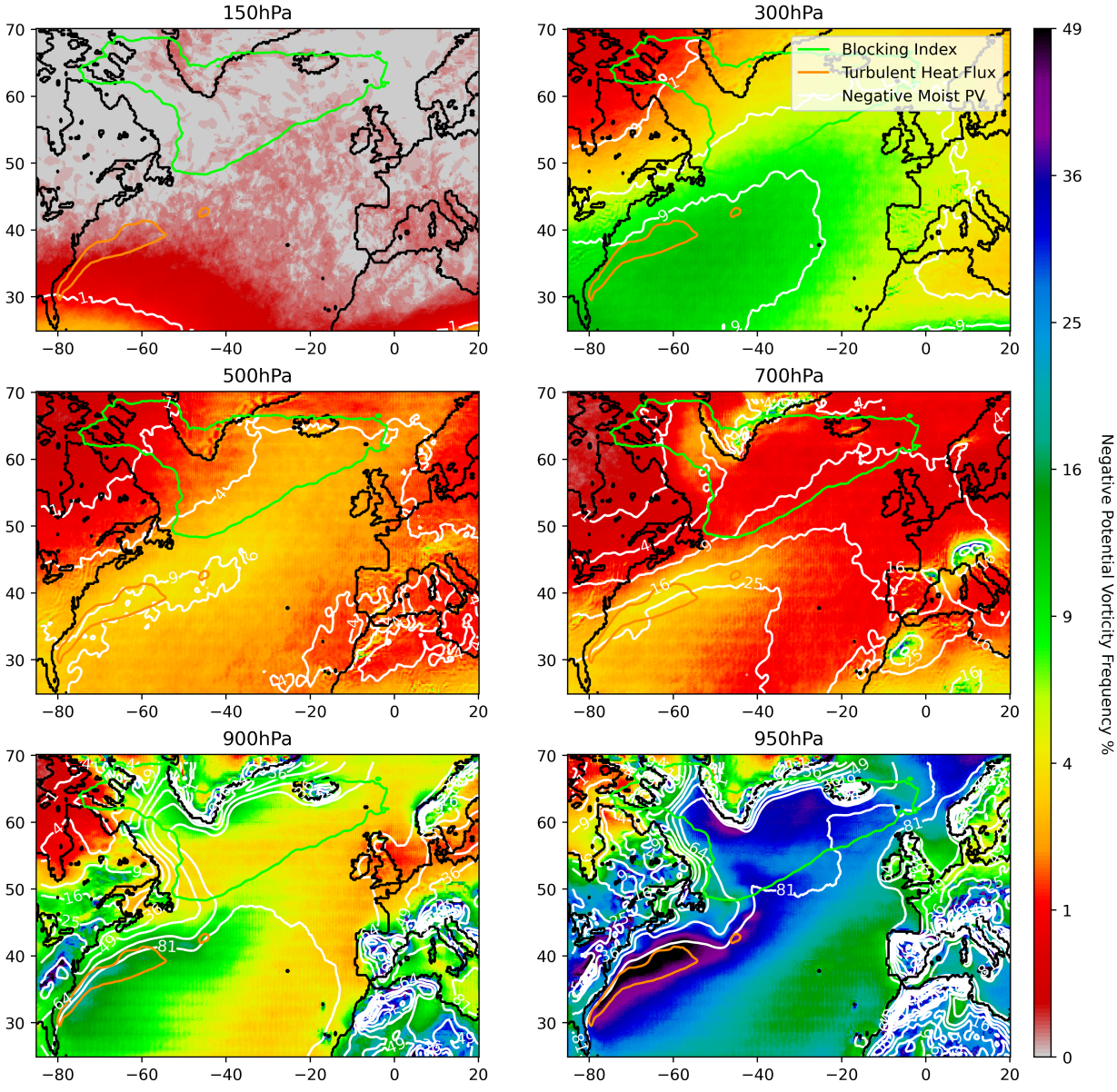

FIG. 4. DJF climatology of the negative PV frequency. The white contours indicate the frequency of negative moist PV. The green and orange contours represent the 7.5% blocking frequency and the 350 Wm^{-2} THF climatology during DJF, respectively.

We now examine the effects of blocking presence over the North Atlantic on these boundary layer processes over the Gulf Stream. Fig. 5 displays a composite of the surface pressure during instances of blocking within the 7.5% DJF blocking frequency climatology contour (green contour) compared to the absence of blocking in this same contour. This composite reveals a high-pressure

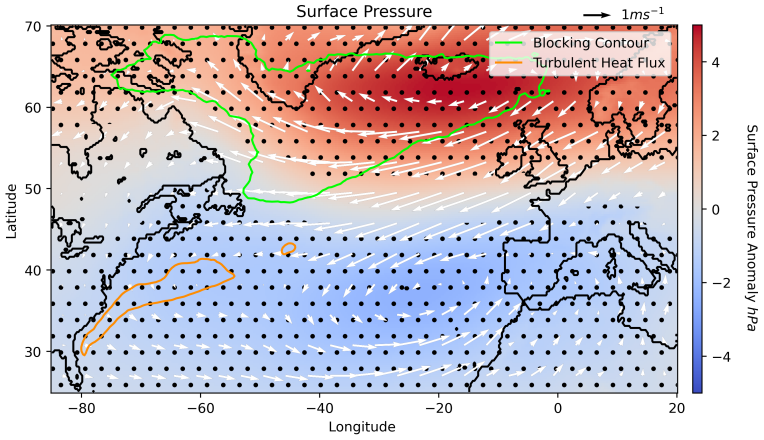

FIG. 5. Surface pressure anomaly (in hPa, color) composite during periods when a block is present inside the green 7.5% DJF blocking frequency climatology contour minus blocking absence in this same contour . The white arrows indicate the 10m wind anomalies, with the black arrow showing the size of the 1m/s vector. The orange contour represents the 350 Wm^{-2} THF climatology during DJF. The stippling indicates 95% confidence.

anomaly centred south of Iceland and a low-pressure anomaly centred on the Azores, indicative of a negative North Atlantic Oscillation (NAO) signal. A negative NAO is associated with weaker westerlies and reduced circulation of warm, moist air from the equator, leading to an increased occurrence of cold air outbreaks across the Gulf Stream (Bjerknes 1964; Cayan 1992; Cellitti et al. 2006; Kolstad et al. 2009), as highlighted by the white arrows denoting anomalous 10m wind. Consequently, a significant increase in THF is observed over the Gulf Stream when blocking is present over the North Atlantic, which coincides with negative PV anomalies in the atmospheric boundary layer over the same region (not shown). Next, we'll investigate how the ocean impacts atmospheric blocking in the North Atlantic and explore the related air-sea interactions, by extending our analysis to summertime months before the winter blocking season.

Oceanic Preconditioning

The top panel in Fig. 6 shows the cross-correlation between the seasonally averaged blocking area time series (refer to Table 1) in DJF and the heat transport time series, depicted in light blue, as well as the heat content time series, depicted in dark orange. The DJF blocking area exhibits a maximum correlation with heat transport through the Straits of Florida five months prior (July, August, September). Since both the heat transport and blocking area time series

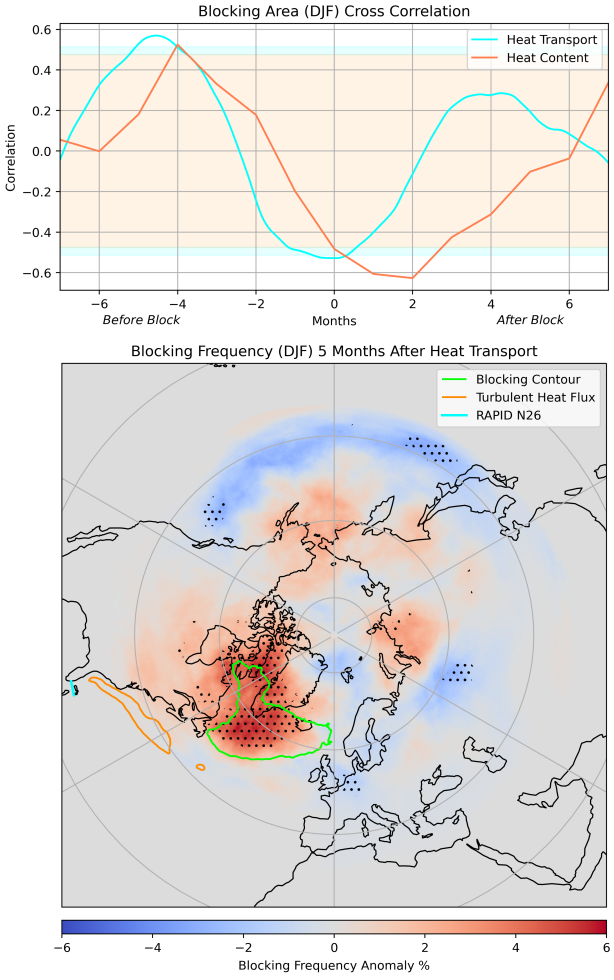

FIG. 6. The top panel shows the cross correlation between the seasonally averaged blocking area time series (refer to Table 1) in DJF and the heat transport (light blue), and the heat content (dark orange) time series. The 95% confidence interval is shown with a coloured fill. The bottom panel shows the composite of the blocking frequency in DJF, 5 months after increased heat transport through the Florida Current. The green and orange contours represent the 7.5% blocking frequency and the 350Wm^{-2} THF climatology during DJF, respectively. The light blue line shows the RAPID N26 mooring. Dotted stippling indicates 95% confidence.

autocorrelations decorrelate far faster than five months, one month and 12 days respectively, this is suggestive of oceanic heat transport forcing the upper troposphere. Simultaneously, there is a notable maximum negative correlation with the heat transport, likely stemming from the wind stress associated with North Atlantic blocking, as observed in Fig. 5, although due to the lack of temporal division, causality is far more difficult to infer. Notably, the strength of this correlation can exceed

0.6, depending on the period in which atmospheric blocking is compared. Examining now the relationship between the heat content and blocking area time series, we observe a maximum positive correlation when the heat content leads by four months, and a maximum negative correlation when it lags by two months. The latter suggests that the block removes heat from the oceanic mixed layer, a relationship similar to that seen by Kelly et al. (2010) between oceanic heat content and THF. The former is consistent with a five month lead seen in the heat transport time series (light blue curve) and a one month time timescale to build this heat anomaly.

The bottom panel in Fig. 6 shows a blocking frequency composite in DJF, five months after increased heat transport through the Straits of Florida. Both the blocking field and heat transport time series are seasonally averaged. This figure demonstrates an increase in atmospheric blocking within the 7.5% DJF blocking frequency climatology (green contour) following increased heat transport in the preceding JAS, with an increase of up to 6%. Additionally, a reduction is observed at lower latitudes around the globe, accompanied by a non-significant positive signal northward of these areas suggestive of northward shift for atmospheric blocks.

To investigate further the heat content change in the ocean, the top panel in Fig. 7 presents a composite of the top 300m ARGO heat content in SON (September, October, November) before a period of increased area blocked inside the green contour. This period corresponds to the time of maximum correlation between ocean heat content and blocking area time series (refer to Table 1) in DJF, as depicted in the upper panel of Fig. 6 (dark orange curve). The composite reveals a statistically significant increase in heat content along the Gulf Stream and its extension. Notably, this signal exhibits a strong resemblance to the SST pattern observed by Rodwell and Folland (2002) with the similar lead time to NAO anomalies. Additionally, this spatial signal is seen when preforming a composite of oceanic heat content in SON using the heat transport time series in the subsequent JAS (not shown).

Conversely, the bottom panel in Fig. 7 displays the same composite of heat content, but in FMA (February, March, April). FMA aligns with the time of maximum negtaive correlation between ocean heat content and blocking area time series (refer to Table 1) in DJF, as shown in the upper panel of Fig. 6 (dark orange curve). This composite exhibits a statistically significant decrease in heat content along the Gulf Stream and its extension, along with a significant increase throughout

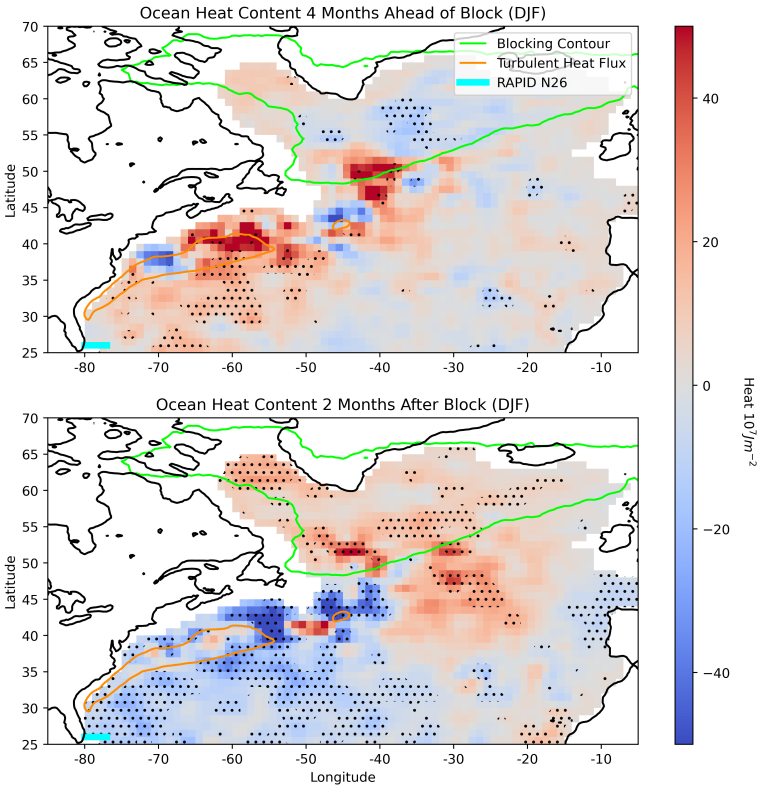

FIG. 7. A composite of the top 300m Argo heat content 4 months before (top panel) and 2 months after (bottom panel) increased blocking area inside the green contour representing the 7.5% blocking frequency climatology during DJF. The orange contours represent the 350Wm^{-2} THF climatology during DJF. The light blue line shows the RAPID N26 mooring. Dotted stippling indicates 95% confidence.

the subpolar gyre. This signal bears resemblance to the well-known SST NAO tripole synonymous with atmospheric forcing (Cayan 1992; Visbeck et al. 2003).

Mechanism

The above results outline the series of events that connects atmospheric blocking to oceanic pathways, and details the coupling between them. This mechanism happens in tandem with dry and moist mechanisms outside of the boundary layer. These results are summarised here in Fig. 8 and are now linked with previously published research in order to describe the mechanism fully.

A number of months prior to a period of increased atmospheric blocking there is increased heat transport through the Florida Straits into the Gulf Stream region. This anomalous heat transport generates surplus heat in this region, which is then entrained into the mixed layer in autumn as

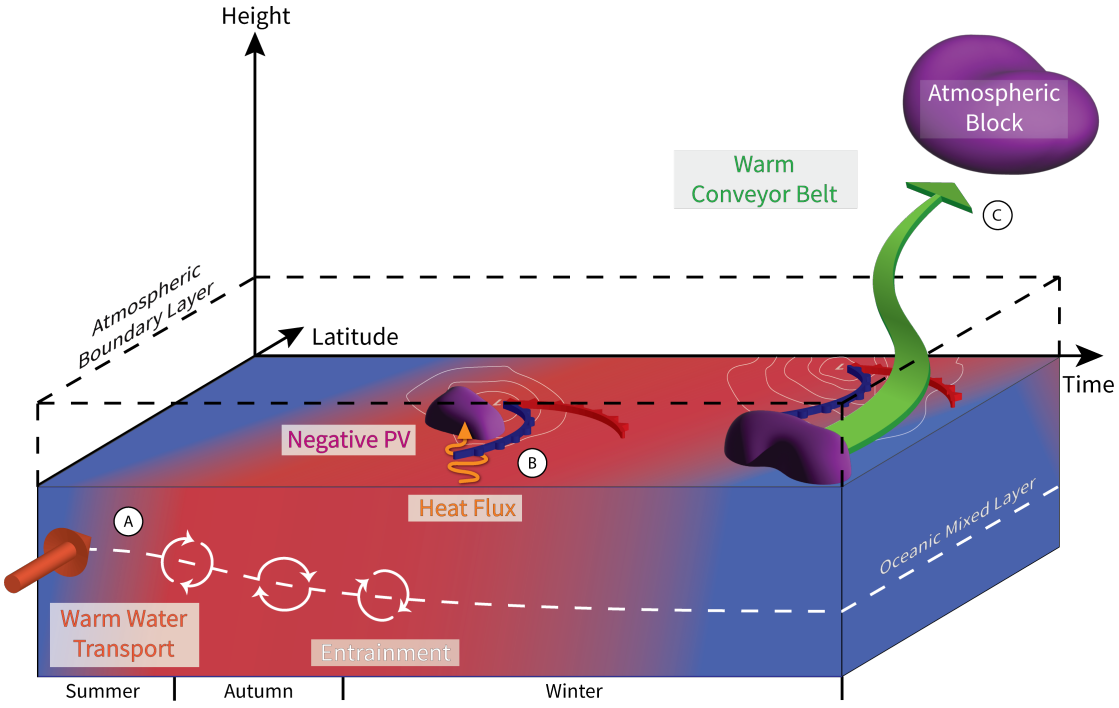

FIG. 8. A schematic summarising the series of events that lead to oceanic maintenance of atmospheric blocking. The bottom slab represents the ocean, with blue and red colors representing anomalously cold and warm water respectively. The red, orange and green arrows show the warm water transport, heat flux from the ocean to the atmosphere and the WCB respectively. The purple blobs show anomalously low PV. Low pressure systems are illustrated with red and blue fronts and grey isobars. The markers A, B, and C are described in the main text.

described by Kraus and Turner (1967), resulting in a larger volume of the ocean becoming available for air-sea interactions (Kelly et al. 2010). This is illustrated in the schematic in Fig. 8 (label **A**).

The surplus heat in the oceanic mixed layer then allows for stronger THF events, as shown by Kelly (2004) and illustrated in Fig. 8 (label **B**). The positive THF seen in Fig. 1 primes the atmospheric boundary layer. Negative PV air masses are generated via the SSHF in the cold sector of the cyclone (Vannière et al. 2016; Attinger et al. 2019) and pool in the wake of this cyclone. Furthermore, these negative PV air masses becomes saturated with moisture due to the intense SLHF in the cold sector. It is important to note that while SLHF doesn't directly affect the PV of the air mass, it does impact the moist PV. As a result, a considerably greater amount of negative moist PV is generated within the boundary layer, as observed in Fig. 2.

Similar to the mechanism described by Papritz et al. (2021), the pooled negative PV air masses are subsequently transported in the WCB of a succeeding cyclone, and injected into the upper troposphere. This contributes to the development of a negative PV anomaly, potentially initiating an atmospheric block, as observed in the middle panel of Fig. 1 and illustrated in Fig. 8 (label **C**).

The moisture from these air masses is utilized for latent heating along the WCB, allowing this air mass to ascend from the boundary layer to the upper troposphere across dry isentropic surfaces, as demonstrated by Madonna et al. (2014). This heating along the WCB increases the "dry" PV below the region of heating and decreases it above (Hoskins 1997). However, from a moist framework, these air masses experience minimal heating as they travel along the WCB, as observed, for example, by Martínez-Alvarado et al. (2014). Therefore, as shown in Fig. 2, the inflow of moist PV is roughly equivalent to the outflow along the WCB. Due to the lack of moisture in the upper troposphere, moist PV is approximately equal to PV, as seen between Fig. 1 and 2 and in Fig. 4, and therefore the PV transported to the block is approximately equal to the moist PV in the boundary layer. In a moist framework, the SLHF serves to steepen moist isentropes, connecting the boundary layer to the upper troposphere. This corroborates with the findings of Sheldon et al. (2017), who suggested that lower Gulf Stream SSTs led to reduced upward transport via WCBs.

Now with the block formed over the North Atlantic, cold dry air is continually advected over the Gulf Stream (Bjerknes 1964; Cayan 1992; Cellitti et al. 2006; Kolstad et al. 2009) as seen in Fig. 5, initiating the positive feedback mechanism that maintains the block. This cold dry air keeps the THF anomalously high, which results in negative PV air masses being repeatedly deposited into the upper troposphere, acting against any decay process within the block (Holmberg et al. 2022). However, this continuous removal of heat from the ocean lowers the heat content, as seen in Fig. 6 (top panel), Fig. 7 (bottom panel), resulting ultimately in a reduced THF. The length of time for this positive feedback to diminish is determined by the amount of surplus heat in the WBC and therefore, the duration of the block is determined, in part, by the oceanic preconditioning. Once the supply of negative or low PV air mass has been cut off, the block begins to decay. This negative feedback process is also seen in Cobb and Czaja (2019) in which the reduction (extension) of the warm core of the Gulf Stream, as a result of consecutive negative (positive) NAO periods, resulted in less (more) negative PV air masses occurring in the atmospheric boundary layer of this

region. The timescale of this negative feedback driven by air-sea interactions in our study is about 3 months.

4. Discussion

Method

In the heat content composite analysis, we observed a strong ENSO signal seen in the Pacific (not shown). As a result, the ENSO 3.4 (Huang et al. 2017) signal was removed from the oceanic heat content fields and the composite time series using a linear regression in order to check whether this had any influence on the composites. We found it did not and we are thus confident that the heat content anomalies seen in Fig. 7 are not related to ENSO variability.

Orders of Magnitude

We now check that the qualitative arguments summarized in Fig. 8 are quantitatively plausible by calculating orders of magnitude for the associated steps. Starting with the oceanic preconditioning, as illustrated in Fig. 8 label **A**, considering that the heat transport time series (refer to Table 1) has a standard deviation of $O(10^{14}\mathrm{W})$ and the heat content anomalies in Fig. 7 (middle panel) are $O(10^{8}\mathrm{Jm}^{-2})$ with an area of $O(10^{12}\mathrm{m}^{2})$, this suggests that the timescales needed to create these oceanic heat anomalies are on the order of months. Analyzing the autocorrelation of the heat transport time series shows this index decorrelating with itself after one month, and hence these heat anomalies are consistent with oceanic heat transport. This oceanic transport timescale is also observed by Hirschi et al. (2019).

Considering the magnitude of the quantities above can give further insight into the amount of negative moist PV that air-sea interactions can generate, as illustrated in Fig. 8 label **B**. The change in moist PV in the boundary layer, ΔQ_e, as a result of heat exchange from the ocean to the atmosphere can be given by (see Appendix):

$$\Delta Q_e = -f\left(\frac{\Delta t_A}{\Delta t_O}\right)\frac{\Delta HC}{C_A(\rho_{BL}h_{BL})^2}, \tag{1}$$

where Δt_A is the timescales an air particle interacts with the WBC $O(10^5\mathrm{s})$, Δt_O is the oceanic timescale $O(10^6\mathrm{s})$ as discussed above and seen in Fig. 6 (top panel), f is the Coriolis parameter

$O(10^{-4}\mathrm{s}^{-1})$, ρ_{BL} is the density of air in the atmospheric boundary layer $O(1\mathrm{kgm}^{-3})$, h_{BL} is the height of the atmospheric boundary layer $O(10^3\mathrm{m})$ and $C_A = 1005\mathrm{Jkg}^{-1}\mathrm{K}^{-1}$ is the specific heat capacity of air. As stated above, the excess heat content per area in the oceanic mixed layer prior to an increased period of blocking, ΔHC, is $O(10^8\mathrm{Jm}^{-2})$. This results in an upper bound on the amount of moist PV generated by excess oceanic heat content of $O(1\mathrm{PVU})$. Approaching this calculation from both an air-sea flux and a warm water transport anomaly perspective (both with orders of magnitude of $O(10^2\mathrm{Wm}^{-2})$ results in the same generation of negative moist PV of $O(1\mathrm{PVU})$. Although this magnitude serves as an upper bound, Fig. 8(d) from Vannière et al. (2016) demonstrated that the generation of negative moist PV in the cold sector is on the order of 1 PVU per day due to THF, a value comparable to that for moist PV.

Finally, considering the moist-adiabatic transport of this boundary layer air mass to the upper troposphere, as illustrated in Fig. 8 label **C**, we can approximate the boundary layer moist PV to the upper-level PV due to the absence of moisture sources upon ascent, i.e., $\Delta Q_e \approx \Delta Q_{Upper}$. Assuming conservation of mass along the WCBs, then the ratio of oceanic contributions to atmospheric blocking can be given by (see Appendix):

$$r = \left(\frac{\Delta P_{BL}}{\Delta P_{Block}}\right)\left(\frac{A_{BL}}{A_{Block}}\right)\left(\frac{\Delta Q_{BL}}{Q_{Block}}\right), \tag{2}$$

where ΔP represents the pressure difference from the bottom to the top of the volume considered, and A is the area of that same volume. Since latent heating does not affect moist PV, and therefore negative moist PV is primarily generated in the boundary layer, examining the white contours in Fig. 4 suggests that approximately $O(10\%)$ of the total boundary layer air mass over the North Atlantic is transported to the upper troposphere. This implies that the area of air mass in the boundary layer that contributes to atmospheric blocking is $A_{BL} \approx O(10^6\mathrm{km}^2)$ which is the same order of magnitude as the area of the block, A_{Block}. Given that the thickness in the block, ΔP_{Block}, is 350hPa, and that of the boundary layer, ΔP_{BL}, is 50-100 hPa, and since the negative anomalies generated in the boundary layer are of the same order of magnitude as the negative PV anomalies in the block $O(1\mathrm{PVU})$, this suggests that oceanic pathways contribute about $r \approx \frac{50-100}{350} \times 1 \times 1 \approx 15\% - 30\%$. This value is remarkably similar to the observations of Yamamoto et al. (2021).

Prediction

By far, the earliest precursor to increased atmospheric blocking over the North Atlantic, as revealed by our study, is the heat transport through the Florida Straits. As shown in the top panel of Fig. 6, the heat transport in JAS (ASO) exhibits a significant correlation with the atmospheric blocking area in DJF (JFM) with a coefficient of 0.57 (0.76 not shown). While the anomalous heat transport shows some dependence on atmospheric forcing via Ekman transport, Hirschi et al. (2019) demonstrated that the volume transport, and consequently the heat transport, through the Florida Straits can primarily be explained by variations in the length of the Loop Current in the Gulf of Mexico. When a vortex is shed by this current into the Gulf of Mexico, the volume of the Loop Current contracts, leading to an increased heat transport through the Florida Straits into the North Atlantic. Astonishingly, this vortex shedding in the Loop Current closely mirrors the wave-breaking process that occurs in the jet stream, ultimately forming atmospheric blocks.

It is important to emphasise that we are not advocating that this process creates a block, rather that it biases the statistics. To draw an analogy, if the occurrence of atmospheric blocks were akin to rolling a dice, oceanic preconditioning effectively changes the dice to a weighted one. Given the high correlation values, this underscores the significance of the Florida Straits heat transport, and possibly the Loop Current, as a source of predictive skill for atmospheric blocking.

5. Conclusion

In this study, atmospheric and oceanic variables were analysed preceding, during and succeeding blocking events using ERA5 (1979-2020), ARGO (2004-2018) and RAPID (2004-2018) data sets. It was shown that:

- Blocking presence over the North Atlantic is linked to increased oceanic heat transport through the Straits of Florida several months prior, followed by an anomalously high oceanic heat content along the Gulf Stream and its extension, and finally with near simultaneous air-sea interactions over the same region.

- The turbulent heat flux over the Gulf Stream and its extension strongly correlates with the PV in the atmospheric boundary layer over the same region. This diabatic process is a major contributor to the generation of negative PV air mass in the boundary layer.

- Negative PV air masses were observed to be transported from the atmospheric boundary layer along the warm conveyor belt of a cyclone to the upper troposphere, where it was found to contribute to the negative PV anomaly of an atmospheric block.

- Air masses with negative PV were observed throughout the troposphere, with the majority of the negative PV present in the boundary layer, followed by 300hPa, and finally the middle troposphere. The reduction in negative PV frequency in the middle troposphere indicates the effects of diabatic processes along the warm conveyor belt. These were not observed when examining negative moist PV frequency.

- We hypothesize that when a block is formed over the North Atlantic, it can feedback positively on itself through the advection of cold dry air over the Gulf Stream, resulting in continued high turbulent heat flux, which maintains the block.

- We further hypothesize that the continued high turbulent heat flux eventually removes the surplus heat from the ocean, which leads to the decay of this air-sea interaction. This severs the atmospheric block from its maintenance pathway, resulting in a negative feedback effect. This suggests that the block's duration is determined, in part, by the surplus heat in the ocean prior to the block.

- Observations suggest a predictive skill in wintertime blocking area arising from the previous summer heat transport by the ocean across the Florida Straits (correlations of 0.6 and higher depending on the period of interest).

It is important to emphasize that, traditionally, atmospheric blocking has been understood within the context of dry and adiabatic quasi-geostrophic dynamics (Shutts 1983). In this view, the ocean's role is limited to introducing only perturbations to this dynamics, which is not inconsistent with our results. Nevertheless, in many studies of this type, Marshall and Molteni (1993) for example, there is an assumed underlying structure of the dynamics, which our study suggests could be attributed to air-sea interactions and could also lend more credence to the view that North Atlantic blocking reflects a fundamentally coupled phenomenon between ocean and atmosphere. Preliminary results from a simple dynamical system model, similar to the work of Palmer (1993), indicate that the different time scales between the atmosphere and the ocean can generate this

intrinsic chaotic behaviour of the coupled system. Ultimately, numerical experiments with high-end climate models are is required to thoroughly test this intriguing new paradigm for atmospheric blocking in the North Atlantic.

Acknowledgments. Thanks to Lukas Papritz and Michael Sprenger for sharing the atmospheric blocking mask for ERA5 as calculated by Schwierz et al. (2004), without which this work would not have been possible.

Discussions with Marta Wenta, Christian Grams, Chris Roberts and Frederic Vitart were greatly appreciated.

This project is part of EDIPI, which has received funding from the European Union's Horizon 2020 research and innovation programme under Marie Sklodowska-Curie grant No. 956396.

Data availability statement. Copernicus Climate Change Service (C3S) (2017): ERA5: Fifth generation of ECMWF atmospheric reanalyses of the global climate . Copernicus Climate Change Service Climate Data Store (CDS), date of access. `https://cds.climate.copernicus.eu/cdsapp#!/home`

Data from the RAPID-MOCHA program are funded by the U.S. National Science Foundation and U.K. Natural Environment Research Council and are freely available at `http://www.rapid.ac.uk/rapidmoc` and `mocha.rsmas.miami.edu/mocha`

These data were collected and made freely available by the International Argo Program and the national programs that contribute to it. (`https://argo.ucsd.edu,https://www.ocean-ops.org`). The Argo Program is part of the Global Ocean Observing System.

APPENDIX

Diabatic Moist PV Generation

The diabatic change in moist potential vorticity is given by:

$$\frac{DQ_e}{Dt} = \frac{f+\zeta_z}{\rho}\frac{\partial \dot{\theta}_e}{\partial z} + \frac{\vec{\zeta_H}.\vec{\nabla}_H \dot{\theta}_e}{\rho}, \tag{A1}$$

where Q_e is moist potential vorticity, $\vec{\zeta}$ is the absolute vorticity, θ_e is the equivalent potential temperature, ρ is the density and z and H indicate the vertical and horizontal components. For air-sea interactions, the first term accounts for the flux from the ocean to the atmosphere while the second term describes the interaction of frontal structures (large horizontal temperature gradients). Average values of ζ_z in the cold sector of cyclones are $O(10^{-5}\mathrm{s}^{-1})$ and therefore, this term will

be ignored due to its small effect relative to the Coriolis parameter. For the purpose of this paper, only the first term on the right hand side of equation A1 will be investigated, i.e.:

$$\frac{DQ_e}{Dt} \approx \frac{f}{\rho}\frac{\partial \dot{\theta}_e}{\partial z}. \tag{A2}$$

The above equation is written in a Lagrangian framework, and therefore the time scales, Dt, considered is the time that an atmospheric particle travels over the WBC, Δt_A. This also implies that the volume being considered is that which is affected by the oceanic heat flux, i.e. the atmospheric boundary layer of height h_{BL}, with moist PV Q_e. In order to link this equation with the observables above, the atmospheric heating in the boundary layer must be introduced. This is given by:

$$\begin{aligned} F_s &= \int_0^{h_{BL}} C_A \rho_{BL} \dot{\theta}_e(z) dz, \\ &= h_{BL} C_A \rho_{BL} \overline{\dot{\theta}_e}, \end{aligned} \tag{A3}$$

where F_s is the turbulent and radiative heat flux from the ocean to the atmosphere, ρ_{BL} is the density of the boundary layer (assumed constant), C_A is the specific heat capacity of air and the bar indicates the average throughout the boundary layer. Making use of Cauchy's mean value theorem between the ocean surface and the top of the atmospheric boundary layer gives the following relation:

$$\overline{\dot{\theta}_e} = \left.\frac{\frac{\partial \dot{\theta}_e}{\partial z}}{\frac{\partial^2 \dot{\theta}_e}{\partial z^2}}\right|_{z=c} \overline{\frac{\partial \dot{\theta}_e}{\partial z}}, \tag{A4}$$

where c is some height between the sea surface and the top of the atmospheric boundary layer. Applying an orders of magnitude argument to the term evaluated at $z = c$ in A4 results in:

$$\overline{\dot{\theta}_e} \approx -h_{BL} \overline{\frac{\partial \dot{\theta}_e}{\partial z}}. \tag{A5}$$

The minus sign is included as the average heating throughout the boundary layer is assumed to be positive and decay with height. Now inserting this relation into equation A3 results in:

$$\overline{\frac{\partial \dot{\theta}_e}{\partial z}} = -\frac{F_s}{C_A \rho_{BL} h_{BL}^2}. \tag{A6}$$

The surface heat flux F_s is sustained by an anomalous ocean heat transport convergence:

$$F_s = \Delta HT. \tag{A7}$$

The latter is what is building up the change in ocean heat content over a timescale Δt_O:

$$\Delta HT = \frac{\Delta HC}{\Delta t_O}. \tag{A8}$$

Approximating the material derivative in equation A2 by overall change, i.e.:

$$\begin{aligned} \frac{DQ_e}{Dt} &\approx \frac{\Delta Q_e}{\Delta t_A} \\ &\approx \frac{f}{\rho_{BL}} \overline{\frac{\partial \dot{\theta}_e}{\partial z}}, \end{aligned} \tag{A9}$$

and combining equations A6, A7 and A8 results in:

$$\Delta Q_e = -f \left(\frac{\Delta t_A}{\Delta t_O} \right) \frac{\Delta HC}{C_A (\rho_{BL} h_{BL})^2}. \tag{A10}$$

We see from this equation that a positive heat content build up relates to the generation of negative moist PV anomalies in the boundary layer. Making use of the hydrostatic balance ($g \rho_{BL} h_{BL} = \Delta P_{BL}$) and relating the change in heat content of the ocean to the change in potential temperature ($\Delta HC = C_O \rho_O h_{ML} \Delta \theta_O$) results in:

$$\Delta Q_e = -\frac{f g \Delta \theta_O}{\Delta P_{BL}} \left(\frac{\Delta t_A}{\Delta t_O} \right) \left(\frac{C_O \rho_O h_{ML}}{C_A \rho_{BL} h_{BL}} \right), \tag{A11}$$

where h_{ML} is the mixed layer thickness of the ocean and ΔP_{BL} is the pressure difference from the bottom to the top of the boundary layer. Notably, the generation of negative moist PV has dependence on latitude through the Coriolis parameter, and on the height of the atmospheric boundary layer, with higher latitudes and shallower atmospheric boundary layers generating more negative moist PV for the same change in heat content, ΔHC. Moreover, a deeper oceanic mixed layer has larger thermal inertia and therefore generates more negative moist PV in the boundary

layer. The ratio of the atmospheric to the oceanic timescales also determines the strength of this interaction, with faster airflow at low level reducing the efficiency of the negative moist PV generation. Additionally, a slow build up of oceanic heat content anomaly also reduces the efficiency of negative moist PV generation.

Considering the moist-adiabatic transport of this lower-level air mass to the upper levels of the atmospheric block, we assume that the boundary layer moist PV is approximately equal to the upper-level PV due to the absence of moisture sources and that mass is conserved along the ascent. Finally, armed with the knowledge of how much boundary layer air mass is transported to the upper troposphere and considering the negative moist PV anomalies generated by the diabatic processes in the boundary layer, we can now estimate the ratio, denoted as r, of the mass integrated PV in the block ($\rho_{Block} V_{Block} Q_{Block}$) to that in the boundary layer, namely:

$$\begin{aligned} r &= \frac{\rho_{BL} V_{BL} \Delta Q_e}{\rho_{Block} V_{Block} Q_{Block}} \\ &= \frac{\Delta P_{BL} A_{BL} \Delta Q_e}{\Delta P_{Block} A_{Block} Q_{Block}}. \end{aligned} \tag{A12}$$

References

Argo, G., 2023: Argo float data and metadata from global data assembly centre (argo gdac). *Seanoe*.

Attinger, R., E. Spreitzer, M. Boettcher, R. Forbes, H. Wernli, and H. Joos, 2019: Quantifying the role of individual diabatic processes for the formation of pv anomalies in a north pacific cyclone. *Quarterly Journal of the Royal Meteorological Society*, **145 (723)**, 2454–2476.

Bennetts, D. A., and B. Hoskins, 1979: Conditional symmetric instability-a possible explanation for frontal rainbands. *Quarterly Journal of the Royal Meteorological Society*, **105 (446)**, 945–962.

Bishop, S. P., R. J. Small, F. O. Bryan, and R. A. Tomas, 2017: Scale dependence of midlatitude air–sea interaction. *Journal of Climate*, **30 (20)**, 8207–8221.

Bjerknes, J., 1964: Atlantic air-sea interaction. *Advances in geophysics*, Vol. 10, Elsevier, 1–82.

Bolton, D., 1980: The computation of equivalent potential temperature. *Monthly weather review*, **108 (7)**, 1046–1053.

Cayan, D. R., 1992: Latent and sensible heat flux anomalies over the northern oceans: The connection to monthly atmospheric circulation. *Journal of climate*, **5 (4)**, 354–369.

Cellitti, M. P., J. E. Walsh, R. M. Rauber, and D. H. Portis, 2006: Extreme cold air outbreaks over the united states, the polar vortex, and the large-scale circulation. *Journal of Geophysical Research: Atmospheres*, **111 (D2)**.

Cobb, A., and A. Czaja, 2019: Mesoscale signature of the north atlantic oscillation and its interaction with the ocean. *Geophysical Research Letters*, **46 (10)**, 5575–5581.

Famooss Paolini, L., P. J. Athanasiadis, P. Ruggieri, and A. Bellucci, 2022: The atmospheric response to meridional shifts of the gulf stream sst front and its dependence on model resolution. *Journal of Climate*, **35 (18)**, 6007–6030.

Frankignoul, C., 1985: Sea surface temperature anomalies, planetary waves, and air-sea feedback in the middle latitudes. *Reviews of geophysics*, **23 (4)**, 357–390.

Frankignoul, C., and K. Hasselmann, 1977: Stochastic climate models, part ii application to sea-surface temperature anomalies and thermocline variability. *Tellus*, **29 (4)**, 289–305.

Gill, A. E., 1982: *Atmosphere-ocean dynamics*, Vol. 30. Academic press.

Häkkinen, S., P. B. Rhines, and D. L. Worthen, 2011: Atmospheric blocking and atlantic multi-decadal ocean variability. *Science*, **334 (6056)**, 655–659.

Haynes, P. H., and M. McIntyre, 1990: On the conservation and impermeability theorems for potential vorticity. *Journal of Atmospheric Sciences*, **47 (16)**, 2021–2031.

Hersbach, H., and Coauthors, 2020: The era5 global reanalysis. *Quarterly Journal of the Royal Meteorological Society*, **146 (730)**, 1999–2049.

Hirschi, J. J.-M., and Coauthors, 2019: Loop current variability as trigger of coherent gulf stream transport anomalies. *Journal of Physical Oceanography*, **49 (8)**, 2115–2132.

Holmberg, E., G. Messori, R. Caballero, and D. Faranda, 2022: The counter-intuitive link between european heatwaves and atmospheric persistence.

Hoskins, B., 1974: The role of potential vorticity in symmetric stability and instability. *Quarterly Journal of the Royal Meteorological Society*, **100 (425)**, 480–482.

561 Hoskins, B., 1997: A potential vorticity view of synoptic development. *Meteorological Applica-*
562 *tions*, **4 (4)**, 325–334.

563 Huang, B., and Coauthors, 2017: Noaa extended reconstructed sea surface temperature (ersst),
564 version 5. *NOAA National Centers for Environmental Information*, **30 (8179-8205)**, 25.

565 Kelly, K. A., 2004: The relationship between oceanic heat transport and surface fluxes in the
566 western north pacific: 1970–2000. *Journal of climate*, **17 (3)**, 573–588.

567 Kelly, K. A., R. J. Small, R. Samelson, B. Qiu, T. M. Joyce, Y.-O. Kwon, and M. F. Cronin, 2010:
568 Western boundary currents and frontal air–sea interaction: Gulf stream and kuroshio extension.
569 *Journal of Climate*, **23 (21)**, 5644–5667.

570 Kolstad, E. W., T. J. Bracegirdle, and I. A. Seierstad, 2009: Marine cold-air outbreaks in the
571 north atlantic: Temporal distribution and associations with large-scale atmospheric circulation.
572 *Climate dynamics*, **33**, 187–197.

573 Kraus, E., and J. Turner, 1967: A one-dimensional model of the seasonal thermocline ii. the general
574 theory and its consequences. *Tellus*, **19 (1)**, 98–106.

575 Madonna, E., H. Wernli, H. Joos, and O. Martius, 2014: Warm conveyor belts in the era-interim
576 dataset (1979–2010). part i: Climatology and potential vorticity evolution. *Journal of climate*,
577 **27 (1)**, 3–26.

578 Marshall, J., and F. Molteni, 1993: Toward a dynamical understanding of planetary-scale flow
579 regimes. *Journal of the atmospheric sciences*, **50 (12)**, 1792–1818.

580 Martínez-Alvarado, O., H. Joos, J. Chagnon, M. Boettcher, S. Gray, R. Plant, J. Methven, and
581 H. Wernli, 2014: The dichotomous structure of the warm conveyor belt. *Quarterly Journal of*
582 *the Royal Meteorological Society*, **140 (683)**, 1809–1824.

583 McCarthy, G. D., and Coauthors, 2015: Measuring the atlantic meridional overturning circulation
584 at 26 n. *Progress in Oceanography*, **130**, 91–111.

585 O'Reilly, C. H., and A. Czaja, 2015: The response of the pacific storm track and atmospheric
586 circulation to kuroshio extension variability. *Quarterly Journal of the Royal Meteorological*
587 *Society*, **141 (686)**, 52–66.

O'Reilly, C. H., S. Minobe, and A. Kuwano-Yoshida, 2016: The influence of the gulf stream on wintertime european blocking. *Climate Dynamics*, **47 (5)**, 1545–1567.

Palmer, T. N., 1993: Extended-range atmospheric prediction and the lorenz model. *Bulletin of the American Meteorological Society*, **74 (1)**, 49–66.

Papritz, L., F. Aemisegger, and H. Wernli, 2021: Sources and transport pathways of precipitating waters in cold-season deep north atlantic cyclones. *Journal of the Atmospheric Sciences*, **78 (10)**, 3349–3368.

Pauluis, O., A. Czaja, and R. Korty, 2010: The global atmospheric circulation in moist isentropic coordinates. *Journal of climate*, **23 (11)**, 3077–3093.

Pfahl, S., C. Schwierz, M. Croci-Maspoli, C. M. Grams, and H. Wernli, 2015: Importance of latent heat release in ascending air streams for atmospheric blocking. *Nature Geoscience*, **8 (8)**, 610–614.

Pfahl, S., and H. Wernli, 2012: Quantifying the relevance of atmospheric blocking for co-located temperature extremes in the northern hemisphere on (sub-) daily time scales. *Geophysical Research Letters*, **39 (12)**.

Rodwell, M., and C. Folland, 2002: Atlantic air–sea interaction and seasonal predictability. *Quarterly Journal of the Royal Meteorological Society: A journal of the atmospheric sciences, applied meteorology and physical oceanography*, **128 (583)**, 1413–1443.

Schwierz, C., M. Croci-Maspoli, and H. Davies, 2004: Perspicacious indicators of atmospheric blocking. *Geophysical research letters*, **31 (6)**.

Sheldon, L., A. Czaja, B. Vannière, C. Morcrette, B. Sohet, M. Casado, and D. Smith, 2017: A 'warm path'for gulf stream–troposphere interactions. *Tellus A: Dynamic Meteorology and Oceanography*, **69 (1)**, 1299 397.

Shutts, G., 1983: The propagation of eddies in diffluent jetstreams: Eddy vorticity forcing of 'blocking'flow fields. *Quarterly Journal of the Royal Meteorological Society*, **109 (462)**, 737–761.

Steinfeld, D., M. Boettcher, R. Forbes, and S. Pfahl, 2020: The sensitivity of atmospheric blocking to upstream latent heating–numerical experiments. *Weather and Climate Dynamics*, **1 (2)**, 405–426.

Steinfeld, D., and S. Pfahl, 2019: The role of latent heating in atmospheric blocking dynamics: a global climatology. *Climate Dynamics*, **53 (9)**, 6159–6180.

Vannière, B., A. Czaja, H. Dacre, T. Woollings, and R. Parfitt, 2016: A potential vorticity signature for the cold sector of winter extratropical cyclones. *Quarterly Journal of the Royal Meteorological Society*, **142 (694)**, 432–442.

Visbeck, M., and Coauthors, 2003: The north atlantic oscillation: climatic significance and environmental impact. *Geophys. Monogr*, **134**.

Wilks, D., 2016: "the stippling shows statistically significant grid points": How research results are routinely overstated and overinterpreted, and what to do about it. *Bulletin of the American Meteorological Society*, **97 (12)**, 2263–2273.

Wilks, D. S., 1997: Resampling hypothesis tests for autocorrelated fields. *Journal of Climate*, **10 (1)**, 65–82.

Woollings, T., and Coauthors, 2018: Blocking and its response to climate change. *Current climate change reports*, **4 (3)**, 287–300.

Yamamoto, A., M. Nonaka, P. Martineau, A. Yamazaki, Y.-O. Kwon, H. Nakamura, and B. Taguchi, 2021: Oceanic moisture sources contributing to wintertime euro-atlantic blocking. *Weather and Climate Dynamics*, **2 (3)**, 819–840.

Yamamoto, A., J. B. Palter, M. S. Lozier, M. S. Bourqui, and S. J. Leadbetter, 2015: Ocean versus atmosphere control on western european wintertime temperature variability. *Climate dynamics*, **45**, 3593–3607.